# Photovoltage and Photocurrent Absorption Spectra of Sulfur Vacancies Locally Patterned in Monolayer MoS$_2$

Alexander Hötger, Wolfgang Männer, Tomer Amit, Daniel Hernangómez-Pérez, Takashi Taniguchi, Kenji Watanabe, Ursula Wurstbauer, Jonathan J. Finley, Sivan Refaely-Abramson, Christoph Kastl, and Alexander W. Holleitner*

ACCESS | Metrics & More | Article Recommendations | SI Supporting Information

**ABSTRACT:** We report on the optical absorption characteristics of selectively positioned sulfur vacancies in monolayer MoS$_2$, as observed by photovoltage and photocurrent experiments in an atomistic vertical tunneling circuit at cryogenic and room temperature. Charge carriers are resonantly photoexcited within the defect states before they tunnel through an hBN tunneling barrier to a graphene-based drain contact. Both photovoltage and photocurrent characteristics confirm the optical absorption spectrum as derived from ab initio GW and Bethe–Salpeter equation approximations. Our results reveal the potential of single-vacancy tunneling devices as atomic-scale photodiodes.
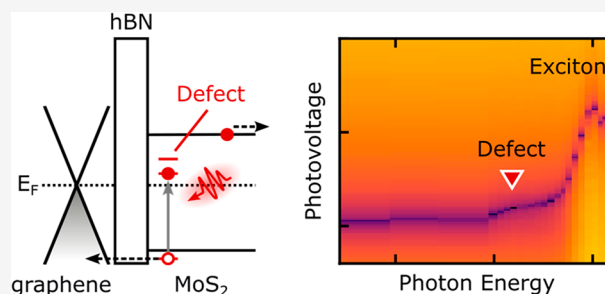
Strong light–matter interactions in atomically thin semiconductors, such as transition-metal dichalcogenides (TMDCs), make them promising materials for efficient solar energy conversion for applications in photodetection, photovoltaics, or photocatalysis.[1,2] Materials with reduced dimensionality allow the exploration of specific and fundamental microscopic effects that are instrumental for the design of the corresponding macroscopic optoelectronic devices. For instance, in two-dimensional (2D) materials, strain engineering can improve the performance of monolayer-based photoabsorbers and thus enable flexible photodetector and solar cell devices with enhanced detection or conversion efficiencies.[3] One-dimensional (1D) geometries, such as in nanowire-based devices,[4] allow the funneling of photogenerated charge carriers into clearly defined current paths. The zero-dimensional (0D) limit can be realized, for example, in quantum-dot configurations, enabling a well-defined spatially localized generation of electron–hole pairs and increased efficiencies due to photogenerated hot carriers.[5,6] Atomistic point defects complement the low-dimensional light-harvesting configurations by introducing a sub-bandgap optical absorption.[7] The latter extends the natural optical absorption spectrum of a given semiconducting crystal to longer wavelengths. However, resolving the impact and the photovoltaic response of a randomly distributed defect in light-harvesting circuits is intrinsically challenging. In this respect, the highly designable 2D layout of TMDC monolayers is a clear advantage. Recently, it was shown that individual single-photon-emitting defect sites can be deterministically generated, e.g., by strain-induced

lateral geometries, where the TMDCs were deposited on arrays of dielectric nanopillars,[8–12] as well as by the impact of focused electron[12–14] and ion beams.[15–20]

We demonstrate that deterministically positioned defects can serve as functional optoelectronic parts of a vertical tunneling van der Waals heterostructure, which effectively acts as a defect-based photodiode. The corresponding sulfur vacancies are generated in monolayer MoS$_2$ by the impact of a focused helium ion beam.[18,20] After resonantly exciting the defects by a laser, we reveal the current of the photoexcited charge carriers across an hBN tunneling barrier and graphene as a drain contact. This MoS$_2$/hBN/graphene heterostructure is an example for vertical tunneling circuits that are particularly advantageous for resolving the small optoelectronic response of localized defect states because of a negligible dark current.[21] The determined photocurrent spectra are consistent with the optical absorption spectrum of monolayer MoS$_2$ with sulfur vacancies, as calculated using the GW and Bethe–Salpeter equation approximation (GW-BSE), which properly accounts for excitonic effects.[22,23] Moreover, we resolve the open-circuit voltage of the defect-based tunneling devices as a function of

the photon energy and find consistent defect-based spectral characteristics. The latter substantiates the interpretation that the optical absorption of the defect states occurs via excitonic states, which are spread across the whole Brillouin zone of $MoS_2$, a result of the structural modifications upon the presence of sulfur vacancies. Our results reveal the pathway of utilizing deterministically generated defects in van der Waals heterostacks for photodiodes. Moreover, the demonstrated finite open-circuit voltage of such nanoscale devices points toward potential solar cell applications based on single to few defects.

Figure 1a sketches the investigated device structure. The heterostacks are fabricated from 2D materials using a dry
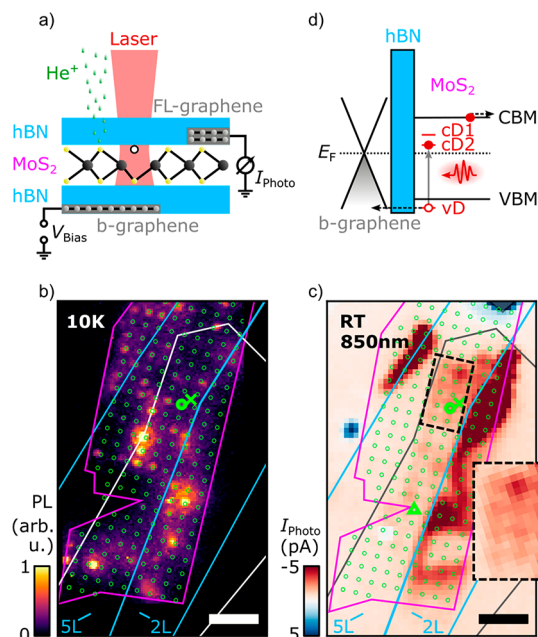


**Figure 1.** Vertical tunneling device with an electrically contacted monolayer $MoS_2$ with sulfur vacancies as generated by a focused He$^+$ ion beam. (a) Sketch of the single sulfur vacancy (white circle) in $MoS_2$ electrically contacted by few-layer (FL) graphene. Photocurrent $I_{photo}$ is measured at a bias $V_{bias}$ across an hBN barrier with graphene as a back-electrode (b-graphene). (b) Low temperature photoluminescence map of a sample with $MoS_2$ (purple), hBN (blue), and b-graphene (white). The hBN is either a quintuple- (5L) or a bilayer (2L). The green array patterns highlight the sites of the focused helium ion beam exposure (equally in (c)). Experimental parameters: photon energy, 2.54 eV; laser power, 10 $\mu$W; bath temperature, 10 K. Scale bar, 5 $\mu$m. (c) Room temperature (RT) photocurrent map with sub-bandgap laser excitation of 850 nm (1.46 eV) at zero bias. Bold circles and triangles (crosses) mark positions at (next to) an exposure site. Scale bar, 5 $\mu$m. (d) Sketch of the vertical band diagram of the $MoS_2$/hBN/b-graphene heterostack. Defect-related states $cD_1$, $cD_2$, and $v_D$ are only located at the sulfur vacancy sites, while the conduction band minimum (CBM) and valence band maximum (VBM) are spatially extended across the $MoS_2$ monolayer.

viscoelastic stamping method. The starting point is a monolayer of $MoS_2$ encapsulated by two hBN layers. The $MoS_2$ is electrically contacted by few-layer graphene (FL-graphene), which represents the ground contact of the tunneling circuit. The bias voltage $V_{bias}$ is applied to a monolayer graphene back-electrode (b-graphene). The tunneling barrier made from hBN between the b-graphene and the monolayer $MoS_2$ consists of sections with quintuple-layers

(5L) and bilayers (2L) (cf. Figure 1b and the Supporting Information). After the assembly, we irradiate the heterostacks with a focused helium ion beam at an acceleration voltage of 30 kV. The irradiation pattern consists of circular patches with a 400 nm diameter oriented in an array with a pitch of 2 $\mu$m (small circles in Figure 1b).[17] The chosen irradiation dose is $1.5 \times 10^{13}$ ions cm$^{-2}$ on each circle (cf. the Supporting Information). Upon ion exposure, single to few sulfur vacancies are generated in the monolayer $MoS_2$ (white circle in Figure 1a).[18,20] To demonstrate the presence of defects in the irradiated $MoS_2$, we measure a low temperature photoluminescence map of the irradiated heterostacks excited with a photon energy above the bandgap of $MoS_2$ (Figure 1b). At each position, we integrate the photoluminescence spectra in an energy range from 1.75 to 1.85 eV, since sulfur vacancies in $MoS_2$ are expected to exhibit a luminescence maximum at ~1.75 eV.[17] Indeed, the photoluminescence maxima in Figure 1b largely coincide with the spatial pattern of the helium ion irradiation (circles). Interestingly, we observe a similar spatial pattern when we measure the photocurrent at energies below the bandgap of $MoS_2$ (cf. Figure 1c). The inset of Figure 1c exemplarily highlights a section of the investigated heterostack with 5L-hBN as a tunneling barrier. Again, the photocurrent maxima largely follow the periodic irradiation pattern of the helium ion exposure. In the following, we discuss the photocurrent dynamics at the exposure sites for the 5L-hBN section and the b-graphene underneath (as in the inset). The obvious differences between the 5L-hBN and 2L-hBN sections as well as between the photocurrent and the photoluminescence map are discussed below and in the Supporting Information.

Figure 1d sketches the band alignment of the vertical tunneling circuit as derived from literature values,[24] with the spatially localized defect conduction band states $cD1$ and $cD2$, the defect valence band state $vD$ within $MoS_2$, and the Fermi level $E_F$ being slightly below $cD1$ and $cD2$.[22,23,25,26] In turn, for a sub-bandgap excitation, optical transitions can occur between $vD$ and $cD2/cD1$ (gray vertical arrow) as well as between the valence band maximum (VBM) of $MoS_2$ and $cD2/cD1$. Since we measure a negative sign of the generated photocurrent at zero bias (cf. Figure 1c), the photoexcited electrons (red circle) propagate laterally within the $MoS_2$ monolayer to the FL-graphene contact, while the holes (white circle) tunnel across the hBN barrier at the position of the defects.

In the following, we compare the photoluminescence spectra measured at the position of a helium ion exposure site (green circles in Figure 1b) to spectra taken next to such a position. At the exposure sites, we observe a luminescence maximum at ~1.77 eV, labeled as $X_{PL}^D$ (black data in Figure 2a); consistent with earlier studies on single sulfur vacancies in $MoS_2$ monolayers.[16,17,25] Next to the exposure sites, we do not detect such maxima within the given noise level (gray data in Figure 2a). On both positions, the A exciton $X_{PL}^A$ has an emission energy of ~1.97 eV, which is consistent with values in pristine $MoS_2$. Intriguingly, the photocurrent spectra deviate from these photoluminescence findings. Namely, the defect-related photocurrent, labeled as $X_{PC}^D$, shows up as an extended contribution at low temperature (cf. red triangle in Figure 2b). We note that Figure 2b shows the photocurrent responsivity vs the excitation energy, i.e., the photocurrent $I_{photo}$ measured as in the sketch of Figure 1a, but normalized to the calibrated excitation power for each laser energy. Hereby, the variation in laser intensity as a function of the excitation energy as well as
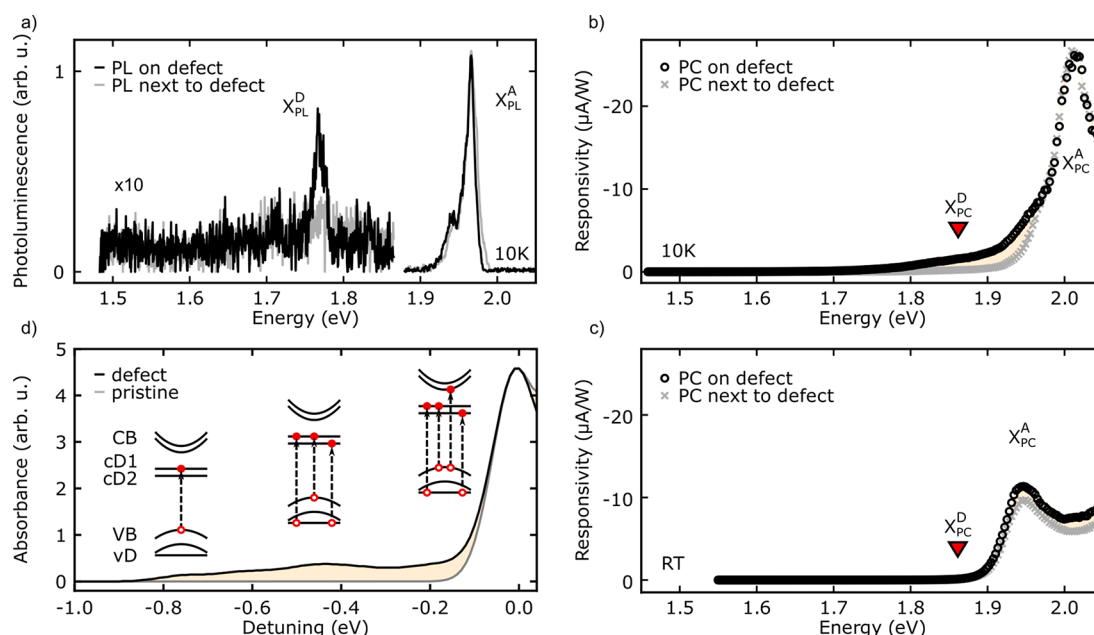
**Figure 2.** Photoluminescence, photocurrent, and theoretical optical absorption spectra. (a) Low temperature photoluminescence on (black) and next to (gray) a sulfur vacancy with a laser excitation energy of 2.54 eV, a laser power of ~10 μW, and a bath temperature of 10 K. Positions correspond to the bold circle and cross in Figure 1b. (b and c) Photocurrent responsivity on (black) and next to (gray) the exposure site at (b) 10 K and (c) room temperature. Positions correspond to the bold circle and cross in Figure 1c. (d) Calculated GW-BSE absorbance of monolayer MoS$_2$ (gray) and with 2% sulfur vacancies (black). Insets: sketched main optical transitions involving defect states. The absorption several hundreds of meV below the A exciton resonance (0.0 eV detuning) results in a mixture of defect and pristine transitions.

chromatic effects within the optical excitation path can be experimentally excluded. We observe that the photocurrent responsivity exhibits a maximum $X_{PC}^A$ at an energy of ~2.01 eV at low temperatures (cf. Figure 2b), which is consistent with the A exciton. Comparing Figure 2b with 2a, $X_{PC}^A$ is shifted to higher photon energies compared to the luminescence maximum $X_{PL}^A$ (~1.97 eV), and the photocurrent maximum is broader in energy. We interpret the energy difference by the Stokes shift between the absorption and emission processes. Moreover, $X_{PC}^A$ shifts to lower energies at higher temperatures (cf. Figure 2c), as it is consistent with a temperature-induced decrease of the bandgap of MoS$_2$. In turn, we deduce that the presented photocurrent spectra relate to the optical absorption process at the examined excitation spots, which also explains the increased width of $X_{PC}^A$ compared to the one of $X_{PL}^A$. For the photocurrent generation, however, relaxation and hot carrier dynamics, as well as the interaction of the photoexcited charge carriers with the thermal baths of electrons and phonons, play an additional role. For instance, at room temperature (Figure 2c), the contribution of $X_{PC}^D$ is hardly resolvable within the given signal-to-noise ratio. At the same time, the photocurrent at the exciton energy $X_{PC}^A$ and above is enhanced at the position of the exposure sites. We explain the enhancement by an interplay of defect states with pristine extended states within the Brillouin zone. Such a hybridization can lead to additional absorption contributions, e.g., via intravalley opposite spin excitations.[23] Since the Fermi energy can be assumed to be only a few meV below cD2 (cf. Figure 1d and refs 25−27), we tentatively suggest that the thermal energy $k_B T_{bath}$, with $k_B$ being the Boltzmann constant, plays the following role. First, at room temperature, the exciton dissociation is more efficient than at cryogenic temperatures,[28] and photogenerated holes are likely to be subject to lateral transport within MoS$_2$, instead of tunneling across the hBN

barrier to the b-graphene. The combination of both processes explains that the overall magnitude of the photocurrent responsivity is reduced in Figure 2c compared with Figure 2b. Second, we argue that the thermal occupation of the underlying defect states becomes relevant at room temperature. In other words, at low temperatures (10 K), cD2 and cD1 can be considered to be unoccupied, and in turn, they can be optically excited from occupied states, such as vD and VB (cf. Figure 1d). At room temperature, however, cD2 and cD1 are occupied by thermal processes, and the optical excitation is effectively shifted to unoccupied states at higher energies. Moreover, single electron occupation dynamics might need to be considered in order to describe the photocurrent spectra in Figures 2b and 2c. Photocurrent spectra of further positions (for the 5L and 2L sections) are provided in the Supporting Information, showing equally the discussed significant sub-bandgap contributions.

Figure 2d depicts the calculated optical absorption spectrum for monolayer MoS$_2$ with sulfur vacancies at a zero temperature. We employ many-body perturbation theory within the GW-BSE approximation.[22,23] The absorption spectrum is calculated for a 5 × 5 periodic supercell containing one sulfur vacancy per cell, corresponding to an effective vacancy density of 2%. For convenience, we shift the spectrum by the values of the peak corresponding to the pristine A exciton, computed to be 2.2 eV. This value is larger than the experimental A peak, as expected due to neglection of surface effects and the corresponding energy renormalization. The pristine monolayer absorption spectrum is also shown for comparison. The finite absorption probability below the optical bandgap of the defect-containing monolayer is attributed to a mixing of defect-to-defect and pristine-to-defect transitions at the sulfur vacancy site (exemplarily sketched in the inset of Figure 2d).[23,25] The presence of defect bands,

which due to state localization are relatively flat and span along the entire Brillouin zone, introduces a wealth of optical electron−hole transitions reflected in a broad active absorption region at energies smaller than the optical bandgap of the pristine monolayer. This effect, clearly observed in comparison to the pristine case in the computed optical absorbance spectrum (Figure 2d), is consistent with the photocurrent spectrum of the exposure sites at low temperatures (Figure 2b). We attribute the measured subgap feature to defect−defect band transitions, mixed with pristine−defect transitions as shown schematically, which appear in the calculated spectra at ∼400 meV below the A transition. Differences from the experimental value of ∼200 meV can be attributed to expected changes in defect band energies upon charging and surface effects, beyond the scope of this work. We show the full calculation of the absorbance with discrete exciton energies and their corresponding oscillator strengths in Figure S7.

Next, we discuss the photovoltage generated in the tunneling device. Figure 3a depicts the absolute value of the photo-
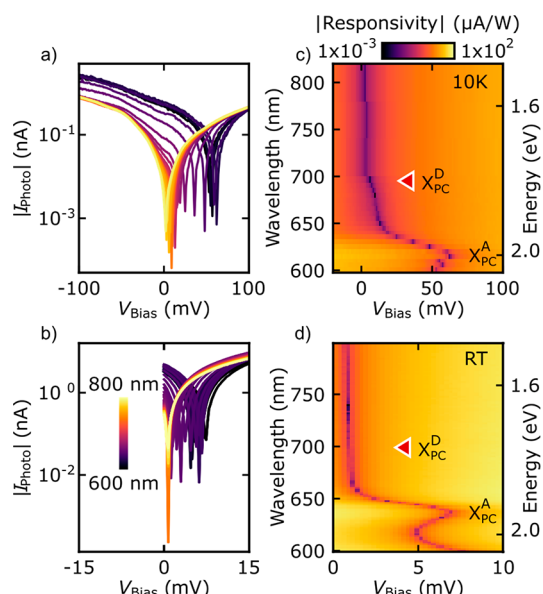


**Figure 3.** Open-circuit photovoltage spectra. (a and b) Logarithmic plot of $|I_{photo}|$ vs $V_{bias}$ at (a) 10 K and (b) room temperature, showing the open-circuit photovoltage as a minimum. (c and d) Corresponding logarithmic responsivity at (c) 10 K and (d) RT. The excitation power is kept constant at 40 μW (50 μW) at each excitation energy for both measurements.

current $|I_{photo}|$ as a function of $V_{bias}$ in a logarithmic scale measured at the position of an exposure site and at a bath temperature of 10 K, while the laser excitation wavelength is varied from 600 to 800 nm (2.06 to 1.55 eV). The minimum of each curve represents the open-circuit voltage $V_{OC}$ of the vertical tunneling circuit for each wavelength (photon energy). The corresponding values of $V_{OC}$ are significantly lower at room temperature (cf. Figure 3b) compared to the values at low temperatures. To understand the difference, we plot the absolute value of the photocurrent responsivity vs $V_{bias}$ in a false-color plot for both temperatures (cf. Figures 3c and 3d). In the chosen logarithmic color scale, the values of $V_{OC}$ show as dark lines as a function of the excitation wavelength (left ordinates) and photon energy (right ordinates). Both, $X_{PC}^D$ and $X_{PC}^A$ are visible in such a representation of the $V_{OC}$ spectrum (Figures 3c and 3d). We note that both $V_{OC}$ spectra

are in nice agreement with the photocurrent spectra, as in Figures 2b and 2c. The similarity can be naively explained by a leading linear dependence of the photocurrent as a function of $V_{bias}$ at a small bias. However, since the value of $V_{OC}$ represents a polarity change of $I_{photo}$ and therefore a minimum of $|I_{photo}|$, the $V_{OC}$ spectra have a greater resolution than the photocurrent spectra (cf. Figures 2b and 2c with Figures 3c and 3d). In particular, $X_{PC}^D$ can now be resolved as a broad sub-bandgap contribution at small values, even at room temperature. Following the arguments from the discussion of the photocurrent spectra, we explain the finite values of $V_{OC}$ at excitation energies below $X_{PC}^A$ as a sub-bandgap optical absorption via collective excitations at the position of the defects.

To explore the photocurrent dynamics within the hybridized defect states in greater detail, we investigated the photocurrent at an exposure site as a function of laboratory time and laser power. Figure 4a shows the temporal characteristics of the
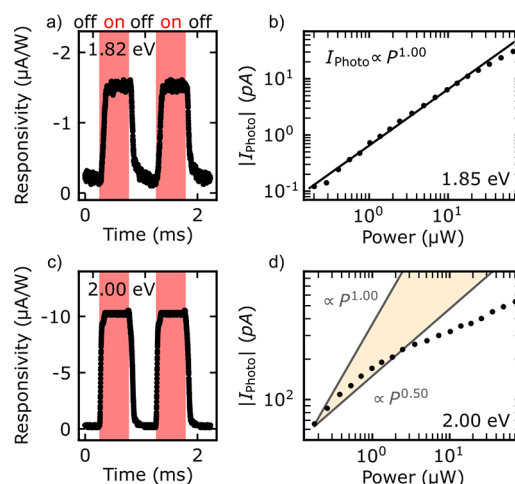


**Figure 4.** Photocurrent dynamics at a sulfur vacancy site. (a and c) Photocurrent responsivity vs lab time measured at an exposure site (cf. triangle in Figure 1c), when the photocurrent is measured at a chopped laser excitation. In (a), the photon energy is below the optical bandgap (1.82 eV), and in (c), it is at the $X_{PC}^A$ resonance (2.00 eV). The red areas highlight the periods during which the laser illumination is on. Power dependence of the photocurrent $I_{photo}$ magnitude at laser excitations of (b) 1.85 eV and (d) 2.00 eV. Solid lines show (sub-) linear power laws. The bath temperature is kept at 10 K.

photocurrent responsivity measured at a sub-bandgap excitation (1.82 eV) for the laser being on/off (red/white areas), while Figure 4b provides the results at an energy resonant to $X_{PC}^A$ (2.00 eV). Both data are taken at $V_{bias} = 0$ V and at $T = 10$ K with the help of an oscilloscope (cf. the Supporting Information). The magnitude is considerably lower for a sub-bandgap excitation (Figure 4a) compared to the resonant excitation (Figure 4b), as it is consistent with the photocurrent spectrum in Figure 2b. Whenever the laser is switched off (white areas in Figures 4a and 4b), the photocurrent drops to zero, and we observe no capacitive currents in the circuits. The decay tails of the photocurrent are on the order of several microseconds, and they are consistent with the finite bandwidth of the utilized current−voltage amplifier. We argue that on each defect position on the MoS₂ monolayer (green circles in Figure 1b), the specific ratio between the characteristic times for luminescence and the photocurrent

determines whether the defect shows up as a maximum in the luminescence (Figure 1b) or in the photocurrent map (Figure 1c). In first order, this explains the difference between the 2L-hBN and the 5L-hBN layers because for the 2L-hBN section, the tunneling times are substantially shorter. However, we still observe bright luminescence in the 2L-hBN section, which we attribute to bubble formation during fabrication. At these specific spots, the monolayer $MoS_2$ might be subject to strain with an additional increase of the separation to graphene, thus enabling localized defect luminescence.[29]

Figure 4c shows the power dependence of $|I_{photo}|$ for a sub-bandgap excitation at an exposure site. For low laser power, $|I_{photo}|$ shows a linear dependence, while at higher power, a saturation behavior sets in for currents above 10 pA. Assuming a pure two-level system, one would expect a saturation current of $|I_{2\text{-level}}| = e \cdot f_{repetion} = 12.5$ pA, with $e$ being the electron charge and $f_{repetion} = 78$ MHz being the repetition frequency of the laser. In this respect, we interpret the slight deviation from a linear behavior at high power as being reminiscent of the dynamics of charge carriers being excited from $vD$ into $cD2$, the latter of which being the lowest unoccupied state within the defect (cf. circles in Figure 1d). This tentative interpretation leaves out the spin-degeneracy of $cD2$, the discussed hybridization with $cD1$ and pristine extended states,[25] and the possibility that more than one defect is involved in the overall dynamics.[17] When we excite at an energy resonant to $X_{PC}^{A}$ ($\sim$2.00 eV) at the exposure sites, we observe a power exponent that is clearly less than unity. This contrasts the expected linear dependence observed in monolayer $MoS_2$ without defects.[30] We explain the sublinear power dependence by an increase of the steady-state Fermi energy upon illumination. In the language of ref 31, trap states of the defect site near $E_F$ are converted to recombination states for the electrons as the laser power is increased. We note that the lateral drift/diffusion dynamics of the photogenerated electrons into the adjacent $MoS_2$ is not sufficiently described by this 3D model.[31] Furthermore, we expect that, at higher excitation power, photogating effects start to carry weight, which further decreases the power exponent.[32,33]

We finally note that the above interpretations are based on sulfur vacancies having the highest occurrence after the helium ion bombardment[20] and that the generation statistics of the luminescent defects can be described by a Poisson distribution.[17] As far as the formation energy of the luminescent defects is concerned, it was demonstrated to be below 1 eV, which is consistent with the luminescent defects being indeed the sulfur vacancies.[18] Importantly, the discussed photocurrent and photovoltage spectra show sub-bandgap contributions, which are consistent with the ab initio calculations of the photon absorption within the sulfur vacancies (Figure 2d). Last but not least, a recent photocurrent experiment on a lateral p−n junction in $WSe_2$ revealed a distinctive sharp photocurrent resonance under resonant excitation of the underlying local excitons.[34] The latter are localized most likely due to an extended strain potential or as defect-bound excitons.[35] Both are not expected to show the spectrally broad sub-bandgap photocurrent responses as discussed here.

In conclusion, we investigated the photocurrent and photovoltage spectra in a monolayer $MoS_2$ tunneling circuit, locally patterned by a helium ion beam. We interpret the results such that the helium ions induce single sulfur vacancies, which show up as luminescence maxima and as a sub-bandgap

contribution to the photocurrent and photovoltage tunneling spectra. The spectra are consistent with ab initio calculations of the optical absorption and excitonic effects computed within the GW and Bethe−Salpeter approximation. Overall, our results pave the way for utilizing single defects in photodiodes based on 2D heterostacks.

## ■ ASSOCIATED CONTENT

### Ⓢ Supporting Information

The Supporting Information is available free of charge at https://pubs.acs.org/doi/10.1021/acs.nanolett.3c03517.

Details on device fabrication and experimental details (photocurrent and photoluminescence) as well as further photocurrent spectra (PDF)

## ■ AUTHOR INFORMATION

### Corresponding Author

**Alexander W. Holleitner** − *Walter Schottky Institute and Physics Department, TU Munich, Garching 85748, Germany;* ⓞ orcid.org/0000-0002-8314-4397; Phone: +49 89 289 11575; Email: holleitner@wsi.tum.de; Fax: +49 89 289 11600

### Authors

**Alexander Hötger** − *Walter Schottky Institute and Physics Department, TU Munich, Garching 85748, Germany*

**Wolfgang Männer** − *Walter Schottky Institute and Physics Department, TU Munich, Garching 85748, Germany*

**Tomer Amit** − *Department of Molecular Chemistry and Materials Science, Weizmann Institute of Science, Rehovot 7610001, Israel*

**Daniel Hernangómez-Pérez** − *Department of Molecular Chemistry and Materials Science, Weizmann Institute of Science, Rehovot 7610001, Israel;* ⓞ orcid.org/0000-0002-4277-0236

**Takashi Taniguchi** − *Research Center for Materials Nanoarchitectonics, National Institute for Materials Science, Tsukuba 305-0044, Japan;* ⓞ orcid.org/0000-0002-1467-3105

**Kenji Watanabe** − *Research Center for Electronic and Optical Materials, National Institute for Materials Science, Tsukuba 305-0044, Japan;* ⓞ orcid.org/0000-0003-3701-8119

**Ursula Wurstbauer** − *Institute of Physics, Westfälische Wilhelms-Universität Münster, Münster 48149, Germany*

**Jonathan J. Finley** − *Walter Schottky Institute and Physics Department, TU Munich, Garching 85748, Germany*

**Sivan Refaely-Abramson** − *Department of Molecular Chemistry and Materials Science, Weizmann Institute of Science, Rehovot 7610001, Israel;* ⓞ orcid.org/0000-0002-7031-8327

**Christoph Kastl** − *Walter Schottky Institute and Physics Department, TU Munich, Garching 85748, Germany;* ⓞ orcid.org/0000-0001-5309-618X

Complete contact information is available at:
https://pubs.acs.org/10.1021/acs.nanolett.3c03517

### Notes

The authors declare no competing financial interest.

## ■ REFERENCES

(1) Ho, W.; Yu, J. C.; Lin, J.; Yu, J.; Li, P. Preparation and Photocatalytic Behavior of $MoS_2$ and $WSe_2$ Nanocluster Sensitized $TiO_2$. *Langmuir* **2004**, *20* (14), 5865−5869.

(2) Wang, Q. H.; Kalantar-Zadeh, K.; Kis, A.; Coleman, J. N.; Strano, M. S. Electronics and Optoelectronics of Two-Dimensional Transition Metal Dichalcogenides. *Nat. Nanotechnol.* **2012**, *7* (11), 699−712.

(3) Gant, P.; Huang, P.; Pérez de Lara, D.; Guo, D.; Frisenda, R.; Castellanos-Gomez, A. A Strain Tunable Single-Layer $MoS_2$ Photodetector. *Mater. Today* **2019**, *27*, 8−13.

(4) Kelzenberg, M. D.; Turner-Evans, D. B.; Kayes, B. M.; Filler, M. A.; Putnam, M. C.; Lewis, N. S.; Atwater, H. A. Photovoltaic Measurements in Single-Nanowire Silicon Solar Cells. *Nano Lett.* **2008**, *8* (2), 710−714.

(5) Nozik, A. J. Quantum Dot Solar Cells. *Phys. E Low-Dimens. Syst. Nanostructures* **2002**, *14* (1−2), 115−120.

(6) Feng, J.; Qian, X.; Huang, C.-W.; Li, J. Strain-Engineered Artificial Atom as a Broad-Spectrum Solar Energy Funnel. *Nat. Photonics* **2012**, *6* (12), 866−872.

(7) Park, J. S.; Kim, S.; Xie, Z.; Walsh, A. Point Defect Engineering in Thin-Film Solar Cells. *Nat. Rev. Mater.* **2018**, *3* (7), 194−210.

(8) Kumar, S.; Kaczmarczyk, A.; Gerardot, B. D. Strain-Induced Spatial and Spectral Isolation of Quantum Emitters in Mono- and Bilayer $WSe_2$. *Nano Lett.* **2015**, *15* (11), 7567−7573.

(9) Kern, J.; Niehues, I.; Tonndorf, P.; Schmidt, R.; Wigger, D.; Schneider, R.; Stiehm, T.; Michaelis de Vasconcellos, S.; Reiter, D. E.; Kuhn, T.; Bratschitsch, R. Nanoscale Positioning of Single-Photon Emitters in Atomically Thin $WSe_2$. *Adv. Mater.* **2016**, *28* (33), 7101−7105.

(10) Palacios-Berraquero, C.; Kara, D. M.; Montblanch, A. R.-P.; Barbone, M.; Latawiec, P.; Yoon, D.; Ott, A. K.; Loncar, M.; Ferrari, A. C.; Atatüre, M. Large-Scale Quantum-Emitter Arrays in Atomically Thin Semiconductors. *Nat. Commun.* **2017**, *8* (1), 15093.

(11) Proscia, N. V.; Shotan, Z.; Jayakumar, H.; Reddy, P.; Cohen, C.; Dollar, M.; Alkauskas, A.; Doherty, M.; Meriles, C. A.; Menon, V. M. Near-Deterministic Activation of Room-Temperature Quantum Emitters in Hexagonal Boron Nitride. *Optica* **2018**, *5* (9), 1128.

(12) Parto, K.; Azzam, S. I.; Banerjee, K.; Moody, G. Defect and Strain Engineering of Monolayer $WSe_2$ Enables Site-Controlled Single-Photon Emission up to 150 K. *Nat. Commun.* **2021**, *12* (1), 3585.

(13) Komsa, H.-P.; Kotakoski, J.; Kurasch, S.; Lehtinen, O.; Kaiser, U.; Krasheninnikov, A. V. Two-Dimensional Transition Metal Dichalcogenides under Electron Irradiation: Defect Production and Doping. *Phys. Rev. Lett.* **2012**, *109* (3), 035503.

(14) Moody, G.; Tran, K.; Lu, X.; Autry, T.; Fraser, J. M.; Mirin, R. P.; Yang, L.; Li, X.; Silverman, K. L. Microsecond Valley Lifetime of Defect-Bound Excitons in Monolayer $WSe_2$. *Phys. Rev. Lett.* **2018**, *121* (5), 057403.

(15) Klein, J.; Lorke, M.; Florian, M.; Sigger, F.; Sigl, L.; Rey, S.; Wierzbowski, J.; Cerne, J.; Müller, K.; Mitterreiter, E.; Zimmermann, P.; Taniguchi, T.; Watanabe, K.; Wurstbauer, U.; Kaniber, M.; Knap,

(16) Barthelmi, K.; Klein, J.; Hötger, A.; Sigl, L.; Sigger, F.; Mitterreiter, E.; Rey, S.; Gyger, S.; Lorke, M.; Florian, M.; Jahnke, F.; Taniguchi, T.; Watanabe, K.; Zwiller, V.; Jöns, K. D.; Wurstbauer, U.; Kastl, C.; Weber-Bargioni, A.; Finley, J. J.; Müller, K.; Holleitner, A. W. Atomistic Defects as Single-Photon Emitters in Atomically Thin $MoS_2$. *Appl. Phys. Lett.* **2020**, *117* (7), 070501.

(17) Klein, J.; Sigl, L.; Gyger, S.; Barthelmi, K.; Florian, M.; Rey, S.; Taniguchi, T.; Watanabe, K.; Jahnke, F.; Kastl, C.; Zwiller, V.; Jöns, K. D.; Müller, K.; Wurstbauer, U.; Finley, J. J.; Holleitner, A. W. Engineering the Luminescence and Generation of Individual Defect Emitters in Atomically Thin $MoS_2$. *ACS Photonics* **2021**, *8* (2), 669−677.

(18) Mitterreiter, E.; Schuler, B.; Micevic, A.; Hernangómez-Pérez, D.; Barthelmi, K.; Cochrane, K. A.; Kiemle, J.; Sigger, F.; Klein, J.; Wong, E.; Barnard, E. S.; Watanabe, K.; Taniguchi, T.; Lorke, M.; Jahnke, F.; Finley, J. J.; Schwartzberg, A. M.; Qiu, D. Y.; Refaely-Abramson, S.; Holleitner, A. W.; Weber-Bargioni, A.; Kastl, C. The Role of Chalcogen Vacancies for Atomic Defect Emission in $MoS_2$. *Nat. Commun.* **2021**, *12* (1), 3822.

(19) Kretschmer, S.; Maslov, M.; Ghaderzadeh, S.; Ghorbani-Asl, M.; Hlawacek, G.; Krasheninnikov, A. V. Supported Two-Dimensional Materials under Ion Irradiation: The Substrate Governs Defect Production. *ACS Appl. Mater. Interfaces* **2018**, *10* (36), 30827−30836.

(20) Mitterreiter, E.; Schuler, B.; Cochrane, K. A.; Wurstbauer, U.; Weber-Bargioni, A.; Kastl, C.; Holleitner, A. W. Atomistic Positioning of Defects in Helium Ion Treated Single-Layer $MoS_2$. *Nano Lett.* **2020**, *20* (6), 4437.

(21) Vu, Q. A.; Lee, J. H.; Nguyen, V. L.; Shin, Y. S.; Lim, S. C.; Lee, K.; Heo, J.; Park, S.; Kim, K.; Lee, Y. H.; Yu, W. J. Tuning Carrier Tunneling in van Der Waals Heterostructures for Ultrahigh Detectivity. *Nano Lett.* **2017**, *17* (1), 453−459.

(22) Refaely-Abramson, S.; Qiu, D. Y.; Louie, S. G.; Neaton, J. B. Defect-Induced Modification of Low-Lying Excitons and Valley Selectivity in Monolayer Transition Metal Dichalcogenides. *Phys. Rev. Lett.* **2018**, *121* (16), 167402.

(23) Amit, T.; Hernangómez-Pérez, D.; Cohen, G.; Qiu, D. Y.; Refaely-Abramson, S. Tunable Magneto-Optical Properties in $MoS_2$ via Defect-Induced Exciton Transitions. *Phys. Rev. B* **2022**, *106* (16), L161407.

(24) Chen, Y.; Huang, S.; Ji, X.; Adepalli, K.; Yin, K.; Ling, X.; Wang, X.; Xue, J.; Dresselhaus, M.; Kong, J.; Yildiz, B. Tuning Electronic Structure of Single Layer $MoS_2$ through Defect and Interface Engineering. *ACS Nano* **2018**, *12* (3), 2569−2579.

(25) Hötger, A.; Amit, T.; Klein, J.; Barthelmi, K.; Pelini, T.; Delhomme, A.; Rey, S.; Potemski, M.; Faugeras, C.; Cohen, G.; Hernangómez-Pérez, D.; Taniguchi, T.; Watanabe, K.; Kastl, C.; Finley, J. J.; Refaely-Abramson, S.; Holleitner, A. W.; Stier, A. V. Spin-Defect Characteristics of Single Sulfur Vacancies in Monolayer $MoS_2$. *Npj 2D Mater. Appl.* **2023**, *7* (1), 30.

(26) Hernangómez-Pérez, D.; Kleiner, A.; Refaely-Abramson, S. Reduced Absorption Due to Defect-Localized Interlayer Excitons in Transition-Metal Dichalcogenide-Graphene Heterostructures. *Nano Lett.* **2023**, *23* (13), 5995−6001.

(27) Hötger, A.; Klein, J.; Barthelmi, K.; Sigl, L.; Sigger, F.; Männer, W.; Gyger, S.; Florian, M.; Lorke, M.; Jahnke, F.; Taniguchi, T.; Watanabe, K.; Jöns, K. D.; Wurstbauer, U.; Kastl, C.; Müller, K.; Finley, J. J.; Holleitner, A. W. Gate-Switchable Arrays of Quantum Light Emitters in Contacted Monolayer $MoS_2$ van Der Waals Heterodevices. *Nano Lett.* **2021**, *21* (2), 1040−1046.

(28) Massicotte, M.; Vialla, F.; Schmidt, P.; Lundeberg, M. B.; Latini, S.; Haastrup, S.; Danovich, M.; Davydovskaya, D.; Watanabe, K.; Taniguchi, T.; Fal'ko, V. I.; Thygesen, K. S.; Pedersen, T. G.; Koppens, F. H. L. Dissociation of Two-Dimensional Excitons in Monolayer $WSe_2$. *Nat. Commun.* **2018**, *9* (1), 1633.

(29) Lorchat, E.; López, L. E. P.; Robert, C.; Lagarde, D.; Froehlicher, G.; Taniguchi, T.; Watanabe, K.; Marie, X.; Berciaud,

S. Filtering the Photoluminescence Spectra of Atomically Thin Semiconductors with Graphene. *Nat. Nanotechnol.* **2020**, *15* (4), 283−288.

(30) Li, Y.; Xu, C. Y.; Wang, J. Y.; Zhen, L. Photodiode-like Behavior and Excellent Photoresponse of Vertical Si/Monolayer $MoS_2$ Heterostructures. *Sci. Rep.* **2014**, *4* (1), 1−8.

(31) Albert, Rose. *Concepts in Photoconductivity and Allied Problems*, no. 19.; Interscience Publishers, 1963.

(32) Hof, K.-D.; Rossler, C.; Manus, S.; Kotthaus, J. P.; Holleitner, A. W.; Schuh, D.; Wegscheider, W. Dynamic Photoconductive Gain Effect in Shallow-Etched AlGaAs/GaAs Quantum Wires. *Phys. Rev. B* **2008**, *78* (11), 115325.

(33) Island, J. O.; Blanter, S. I.; Buscema, M.; van der Zant, H. S. J.; Castellanos-Gomez, A. Gate Controlled Photocurrent Generation Mechanisms in High-Gain In2Se3 Phototransistors. *Nano Lett.* **2015**, *15* (12), 7853−7858.

(34) Paur, M.; Molina-Mendoza, A. J.; Polyushkin, D.; Michaelis De Vasconcellos, S.; Bratschitsch, R.; Mueller, T. Resonant Photocurrent from a Single Quantum Emitter in Tungsten Diselenide. *2D Mater.* **2020**, *7* (4), 045021.

(35) Chen, Y.; Liang, H.; Loh, L.; Ho, Y.; Verzhbitskiy, I.; Watanabe, K.; Taniguchi, T.; Bosman, M.; Bettiol, A. A.; Eda, G. Gate-Tunable Bound Exciton Manifolds in Monolayer $MoSe_2$. *Nano Lett.* **2023**, *23* (10), 4456−4463.